

RESEARCH ARTICLE | MAY 22 2025

Influence of swirl ratio on the structure and dynamics of tornado-like vortices

SCI F

Soohyeon Kang; Rajesh Ramesh; Yulia Peet ; Leonardo P. Chamorro

Check for updates

Physics of Fluids 37, 057135 (2025)
<https://doi.org/10.1063/5.0270056>



Articles You May Be Interested In

Call Dorothy! Researchers identify how a tornado's 'swirl ratio' affects its structure and motion

Scilight (May 2025)

Coherent structures in tornado-like vortices

Physics of Fluids (August 2019)

Towards the development of analytical tornado-like models

AIP Advances (December 2018)



Physics of Fluids
Special Topics
Open for Submissions

[Learn More](#)

 AIP
Publishing

Influence of swirl ratio on the structure and dynamics of tornado-like vortices

F SCI

Cite as: Phys. Fluids 37, 057135 (2025); doi: 10.1063/5.0270056

Submitted: 9 March 2025 · Accepted: 9 April 2025 ·

Published Online: 22 May 2025



View Online



Export Citation



CrossMark

Soohyeon Kang,¹ Rajesh Ramesh,² Yulia Peet,² and Leonardo P. Chamorro^{1,3,4,5,a}

AFFILIATIONS

¹Mechanical Science and Engineering, University of Illinois, Urbana, Illinois 61801, USA²School for Engineering of Matter, Transport and Energy, Arizona State University, Tempe, Arizona 85287-6106, USA³Civil and Environmental Engineering, University of Illinois, Urbana, Illinois 61801, USA⁴Aerospace Engineering, University of Illinois, Urbana, Illinois 61801, USA⁵Earth Science and Environmental Change, University of Illinois, Urbana, Illinois 61801, USA^aAuthor to whom correspondence should be addressed: lpchamo@illinois.edu

ABSTRACT

We investigated the flow dynamics of tornado-like vortices, examining the influence of swirl ratio, S , defined as the ratio of tangential to radial momentum at the vortex base, on their structural characteristics. Using a combination of particle image velocimetry (PIV) in a custom-built simulator and large-eddy simulations (LES), we analyzed vortex flows at swirl ratios of $S = 4.66$, 1.25 , and 0.33 . The results demonstrate that vortex flow characteristics strongly depend on S , with improved agreement between experimental and numerical data when employing flow-based swirl ratio definitions. Vortex wandering was quantified in experiments, and corrections were applied to refine tangential and radial velocity profiles. At $S = 0.33$ and 1.25 in experiments and $S = 1.25$ and 4.66 in simulations, the vortex transitioned from a single-celled to a double-celled structure, with further evolution into multi-celled vortices at the highest swirl ratio, substantially modifying circulation patterns. Proper orthogonal decomposition (POD) characterized the coherent structures governing vortex dynamics and their dependence on swirl ratio, revealing distinct physical features associated with each vortex regime.

Published under an exclusive license by AIP Publishing. <https://doi.org/10.1063/5.0270056>

28 May 2025 01:37:14

I. INTRODUCTION

Wind-borne debris is often transported by concentrated vortices, such as tornadoes, presenting a substantial hazard to human life and the structural stability of buildings. In 2011, tornadoes resulted in 158 casualties and \$9.6 billion in damages in the United States.¹ The damage inflicted by the top 1% of the most costly tornadoes has shown an increasing trend from 1970 to 2023, particularly in the Southeast US and the Upper Midwest US. Over this period, the proportion of damage caused by these severe tornadoes has approximately doubled and tripled, respectively, highlighting a significant escalation in their economic impact.² Given the devastating nature of tornadoes, characterizing their features and the dynamics of flow fields is critical to minimizing potential harm. Consequently, a comprehensive examination of tornadoes has been undertaken through various methodologies, including full-scale observations,^{3–6} physical modeling,^{7–10} and numerical simulations.^{11–14}

In recent decades, Doppler radar technologies have become prevalent for capturing full-scale observations of tornadoes. The advent of Doppler on Wheels (DOW)¹⁵ has enabled rich collection of tornado

data throughout their entire lifespan from a safe distance. Nonetheless, acquiring *in situ* measurements remains challenging due to the unpredictable and highly destructive nature of tornadoes, highlighting the necessity of the laboratory tornado simulators.

Ying and Chang¹⁶ conducted the first experimental study on tornado-like vortices using a physical simulator with a rotating cylindrical screen inducing circulation above the ground and a suction fan for axial flow. Ward⁸ later improved this design with the development of the Ward-type Tornado Vortex Chamber. This simulator features a convergence chamber with a rotating mesh screen, which can control the circulation, and a convection chamber including a fan positioned atop with a honeycomb structure below it, providing a realistic boundary condition. In 2008, Haan *et al.*⁹ developed a tornado simulator in Iowa State University, which generates a vortex that can move along a ground plane. This simulator, suspended from a crane, uses a 1.83 m diameter fan to create rotating downdraft, which is directed by guide vanes to impart angular momentum. More recently, the Wind Engineering Energy and Environment (WindEEE) dome was built at the Western University in Canada, which comprises a 40 m outer

diameter hexagonal chamber with 100 dynamic fans along its six peripheral walls and 6 larger fans positioned at the top.^{17,18} This facility allows for the study of various large-scale vortex structures by adjusting guide vanes in front of the fans at the lower levels.

Numerical simulations of tornado-like vortices have also been conducted. Early numerical studies assumed a two-dimensional, axisymmetric flow model driven by vertical and rotational forcing.^{11,19,20} They solved the Navier-Stokes equations in a two-dimensional axisymmetric domain without invoking any turbulence model. Lewellen *et al.*²¹ were the first to consider large-eddy simulations (LES) in a three-dimensional domain in application to tornado-like flows. The LES approach was followed by a number of researchers^{13,14,22–24} and has proven to be successful in reproducing main physical characteristics observed in realistic tornado-like vortices.^{13,22} Most of the numerical studies of tornado-like vortices have been performed in idealized cylindrical domains.^{12–14,21,22,24} Some recent attempts to simulate a full setup of representative laboratory tornado simulators with guide vanes included via Reynolds-averaged Navier-Stokes (RANS)²⁵ and LES²³ approaches can also be acknowledged.

While the mean flow fields, turbulent properties, and coherent vortex structures reproduced in different experimental configurations and numerical setups were reported to have common features, detailed flow characteristics including the number of observed vortices did not necessarily match. To scale the flow characteristics between different realizations, two nondimensional parameters emerged as significant: (1) the swirl ratio, S , which describes the ratio of tangential momentum to radial momentum in the flow,^{9,26,27} and (2) the radial Reynolds number,^{9,17,28} $Re_r = Q/2\pi h\nu$, where Q/h is the volumetric flow rate (Q) per unit axial length (h), and ν is the kinematic viscosity of the fluid. While swirl ratio has been shown to be a central parameter characterizing the structure of the vortex flows, the effect of the radial Reynolds number has proven to be secondary. Indeed, with a sufficiently high value of Re_r , typical of a turbulent vortex, previous studies observed that the effect of the radial Reynolds number on the vortex structure and the vortex transitions becomes minimal.^{18,28} We note, however, that Re_r can still exert some influence on the flow even past its critical value as demonstrated in a recent study by Zhao *et al.*²⁴ who observed that quantitative characteristics of the vortex core, such as core radius and maximum tangential velocity, can still be affected by the radial Reynolds number in a post critical regime.

Swirl ratio has been shown to affect the major flow characteristics, including the vortex core radius, maximum tangential velocity, vortex wandering, and the number of coherent vortex structures observed in the flow. It was established with reasonable confidence that an increase in the swirl ratio results in an increase in the vortex core radius.^{8,24,26,29–31} The effect of the swirl ratio on the maximum tangential velocity was less evident, with a recent numerical study by Zhao *et al.*²⁴ showing that an increase in the swirl ratio resulted in a reduced maximum tangential velocity, while experimental studies by Tang *et al.*³⁰ and Lv *et al.*³¹ reported opposite trends. Experimental studies by Zhang and Sarkar,³² Refan and Hangan,¹⁷ and Lv *et al.*³¹ also showed that large swirl ratios suppress vortex wandering. Vortex wandering represents a major issue in interpreting statistical results of the vortex flow measurements,^{17,31–34} especially in the large-scale and open-type vortex simulators, where vortex wandering is significant.

Ward⁸ and Jischke and Parang²⁹ were the first to discuss the vortex structure evolution as a function of the swirl ratio, noting the

transition from a single to multiple vortex structures with an increasing swirl ratio, a phenomenon further evidenced in subsequent studies.^{17,28,34} While this phenomenon was qualitatively reproduced in various setups, Haan *et al.*⁹ reported that the exact values of the swirl ratios at which transition from single to multiple structures occurred differed between the original Ward-type simulator^{8,29} and the large-scale open-type facility that they built at ISU to simulate moving vortices.^{9,32} To reconcile this, Haan *et al.*⁹ proposed a different definition of the swirl ratio that is based on local flow variables (flow based swirl ratio) rather than on purely geometrical parameters (geometric swirl ratio) as defined originally in Davies-Jones.²⁶ This new definition seemed to provide a better scaling between different setups.^{13,32} Several more definitions of swirl ratios and governing non-dimensional parameters (e.g., the vortex Reynolds number^{11,35}) have been proposed in an attempt to reconcile between different vortex flow realizations obtained under different setups and boundary conditions.^{14,17,26,36,37} Clearly, the issue of comparison and reproducibility of different vortex conditions among different experimental and numerical configurations remains an open question.

The current study is concerned with the ability of a joint experimental and numerical campaign to establish comparable vortex flow conditions of a small-scale prototype vortex modeled in a laboratory simulator and in a large-eddy simulation model. Joint experimental and numerical investigations provide an opportunity to probe distinct features of complex flow phenomena in a coordinated and complementary manner, which is critical for advancing our understanding of vortex flows and atmospheric modeling. Despite a large number of experimental and numerical investigations performed on tornado-like vortices, they were all conducted in isolation, and attempts for coordinated joint experimental and numerical studies are largely lacking. While the importance of validation of numerical simulations of tornado vortices with laboratory and field measurements has been discussed,^{12,13,23,25} available comparisons document mean normalized velocity and pressure profiles at certain heights.^{12,13,23,25} A joint description of three-dimensional turbulent flow fields and vortex structures between experiments and simulations under the matched flow conditions is still lacking.

In this study, we built a small-scale vortex simulator to generate tornado-like vortices in the laboratory and investigated distinct flow fields using particle image velocimetry (PIV), focusing on varying swirl ratios. Complimentary numerical simulations using LES in a high-order spectral-element method were carefully designed in coordination with experimental studies with the goal of matching experimental conditions to the best extent possible while allowing for certain idealizations that cannot be avoided with LES modeling approaches. We put a special emphasis on highlighting the similarities and differences between experimental and numerical results regarding mean flow fields, turbulence statistics, and the three-dimensional vortex structure, including vortex wandering, vortex breakdown, number of coherent vortices observed, and a transition between different flow regimes as influenced by the swirl ratio. We also discuss the reasons for a possible disagreement between experiments and simulations and emphasize the influence of the limitations in experimental and numerical setups with respect to establishing comparable vortex flow fields.

Basic details of the experimental simulator and the PIV setup are provided in Sec. II. Section III presents the description of the numerical simulations and the computational methodology. Experimental

and numerical results, including time-averaged flow characteristics, vortex wandering, and analysis of vortex structures, are described in Sec. IV. Section V provides a discussion of the results in the context of the previous literature and analyzes applicability of different swirl ratio definitions to the interpretation of the current findings. Section VI formulates the conclusions of the study.

II. EXPERIMENTAL SETUP

Experiments were conducted in a facility specifically designed to generate customized vortex-type flows with varying strengths, whose axes coincide with the vertical coordinate. The vortex simulator produces a rotational shear flow at the bottom wall, induced by 18 adjustable fans, each 80 mm in diameter, arranged in a hexagonal pattern. Each fan has a rated flow rate of 32.28 CFM at 12 V and operates at 10 V in the current experiments. Based on these specifications, the total flow rate into the domain from 18 fans is calculated as $Q = 0.234 \text{ m}^3/\text{s}$. In front of the fans, 25 vanes are uniformly spaced around the perimeter of a 400 mm diameter circumference to guide the inflow. Above this arrangement, a large suction fan, 400 mm in diameter, creates an upward axial flow. This flow is straightened by a honeycomb-type grid positioned directly below the fan, which can be adjusted in height but was set at $H = 450 \text{ mm}$ above the bottom wall for this study. The simulator is open on all sides, with only four aluminum profiles at each corner providing structural support. The thickness of these supports is comparatively small, and their distance from the vortex generation system is sufficiently large to minimize any effects on the dynamics of the vertically oriented vortex. The flow is mechanically driven by boundary forcing, with no intentional thermal gradients introduced. The laboratory environment is maintained at a uniform ambient temperature, and no heat sources or sinks are present within the test section. As such, temperature-induced baroclinic effects are expected to be negligible. A basic schematic of the vortex simulator illustrating the main features is shown in Fig. 1.

Three distinct vortex regimes were characterized by adjusting the vane angles to $\theta = 75^\circ$, 45° , and 15° , respective to the radial line to the center. The selected angles resulted in swirl ratios $S = (2a)^{-1} \tan \theta$, where a represents the ratio of the inflow height (80 mm) to the top fan radius (200 mm), of $S = 4.66$, 1.25 , and 0.33 . Here, we use a geometric definition of the swirl ratio as originally presented by Davies-Jones.²⁶ This definition uses purely geometric parameters and allows us to match experimental and numerical conditions *a priori*. Other definitions of the swirl ratio which use the flow field values can only be measured *a posteriori*^{9,17,32} and could not be chosen as a controlled parameter to match experimental and numerical conditions during the setup phase. Relationships between the geometric swirl ratio and the other flow-based definitions in the context of the current results are discussed in Sec. V.

Given the fixed flow rate into the domain ($Q = 0.234 \text{ m}^3/\text{s}$) and the fixed inflow height ($h = 80 \text{ mm}$), the radial Reynolds number was held constant in experiments at $Re_r = 3.1 \times 10^4$ for the three swirl ratios. The vortex flows were characterized using particle image velocimetry (PIV) across two perpendicular planes: one wall-parallel and the other vertical. Wall-parallel measurements were taken at a plane 120 mm above the bottom wall. Vertical measurements were taken at a plane perpendicular to the bottom wall and intersecting the center of the simulator. Two fields of view (FOV) were considered in the horizontal plane: one covering an area of $x \in [-84 \text{ and } 84 \text{ mm}]$ and $y \in [-52 \text{ and } 52 \text{ mm}]$ (FOV1), and the other covering $x \in [-15 \text{ and } 190 \text{ mm}]$ and $y \in [-62 \text{ and } 62 \text{ mm}]$ (FOV2), where the origin of the coordinate system $(x, y) = (0, 0)$ is located at the center of the simulator. For the vertical plane, the field of view covered $x \in [-80 \text{ and } 150 \text{ mm}]$ and $z \in [150 \text{ and } 400 \text{ mm}]$ (FOV3), where z is the vertical coordinate with its origin at the bottom wall.

Green-dyed water droplets with a diameter of $1 \mu\text{m}$, generated by ultrasonic compressors positioned behind the bottom fans, were used to seed the flow and were illuminated by a pulsed laser with a

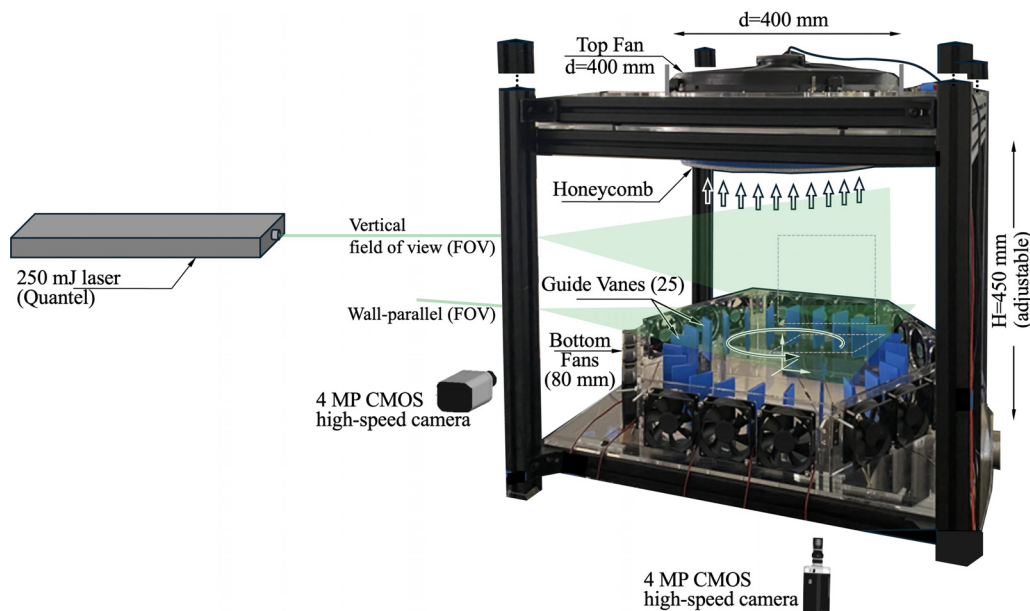


FIG. 1. Basic schematics of the tornado-like vortex simulator illustrating core components and the horizontal and vertical field of views.

wavelength of 532 nm. The corresponding particle Stokes number, $St \ll 1$, ensured that the particles accurately followed the flow, behaving as effective tracers at the measured scales. The particle images were captured by a 4 MP high-speed CMOS camera with a sampling frequency of 14 Hz. The velocity fields were obtained through cross correlation between pairs of images, where the interrogation window size was 32×32 pixels² with a 50% overlap, resulting in a spatial resolution of $\Delta x = \Delta y = 1$ and 2.4 mm, depending on the field of view.

III. NUMERICAL METHODOLOGY

The numerical simulations of the vortex-type flow generated by the vortex simulator are performed using large-eddy simulations (LES) with a high-order open-source computational fluid dynamics (CFD) solver, Nek5000.³⁸ It employs a spectral element methodology to solve the incompressible Navier–Stokes equations. Spectral element method is a high-order weighted residual technique in which the spatial domain is discretized into a collection of hexahedral tensor-product elements.³⁹ Within each element, the solution is represented in terms of N th-order tensor-product polynomials where the basis functions are Lagrange (nodal) polynomials based on the Gauss–Lobatto–Legendre (GLL) quadrature points.

For the numerical simulations, we use a cylindrical domain with the height of 450 mm and the radius of 200 mm that matches the dimensions of the experimental setup. The bottom fans with guide vanes are modeled using an inlet condition with both normal and tangential velocity components. The bottom surface is taken as a wall with no-slip boundary condition. The lateral boundary of the cylindrical domain is an inlet boundary from $z = 0$ to $z = 80$ mm based on the experimental fan dimensions. From $z = 80$ to $z = 450$ mm, the lateral boundary is a symmetric (slip-wall) boundary based on the assumption that most of the flow exits via the outlet at the top surface where the top fan is located, which was confirmed by experimental observations. The top boundary is set up as an outflow boundary of the domain. An illustration of the domain geometry and boundary conditions is provided in Fig. 2. As in experiments, temperature effects are not considered in the current numerical study, and the fluid density is assumed constant.

We set the inlet horizontal velocity magnitude $|v|_{inlet}$ constant between the cases and specify the radial and tangential inlet velocities as $v_{r,inlet} = |v|_{inlet} \cos \theta$ and $v_{\theta,inlet} = |v|_{inlet} \sin \theta$, where θ is the guide vane angle. As in the experiments, three distinct vortex flow regimes

are considered, with the vane angles specified as $\theta = 75^\circ$, 45° , and 15° . Given the same inflow height of $h = 80$ mm as in the experiments, this gives the swirl ratio values as $S = 4.66$, 1.25 , and 0.33 matching the experimental conditions. The value of the horizontal velocity magnitude $|v|_{inlet}$ was determined for the simulations to yield equivalent rotational flowfields as in the experiments (with maximum tangential velocities $v_{\theta,max}$ between 2 and 3 m/s, see Figs. 3 and 8). It was found that the value of $|v|_{inlet} = 1.4$ m/s provides this match reasonably well and was used in simulations. This sets the radial Reynolds numbers in the simulations as $Re_r = 4.9 \times 10^3$, 1.3×10^4 , and 1.8×10^4 for the swirl ratios of $S = 4.66$, 1.25 , and 0.33 . We note that, while these radial Reynolds numbers are somewhat smaller than in the experiments, they are still above the critical value ($Re_{r,cr} \approx 4.1 \times 10^3$, see Church *et al.*²⁸) above which transition between vortex structures is presumed to be independent of the radial Reynolds number.^{17,28,31}

The cylindrical computational domain is discretized using the O-grid technique involving structured hexahedral elements. The resulting mesh consists of 2816 elements. We use $N = 7$ for the polynomial order of approximation to represent the solution inside each element, which yields approximately 1.4×10^6 grid points for the entire domain. The grid is stretched along the wall-normal direction so that the spacing near the wall is within one wall unit, justifying the use of the wall-resolved LES. The grid spacing is nearly uniform in the wall-parallel plane and ensures a sufficient grid spacing to resolve the horizontal motions created by the vortex in the near-wall and the outer layers of the flow. For the subgrid-scale model in large-eddy simulations, we use high-order polynomial filtering as a regularization model which effectively acts as a subgrid scale dissipation on the LES grid.^{40,41}

IV. RESULTS

A. Mean flow characteristics

Time-averaged flow characteristics in the horizontal plane at $z = 120$ mm for three swirl ratios, $S = 4.66$, 1.25 , and 0.33 obtained from experiments, are illustrated in Fig. 3. Considering the motion of the vortex center, we adjusted the spatial coordinates to align the origin with the instantaneous vortex center in each snapshot for the time-averaged calculation. This was done using the transformations $x' = x - x_c$ and $y' = y - y_c$, where (x_c, y_c) denotes the location of the instantaneous vortex center. The location of the vortex center at any

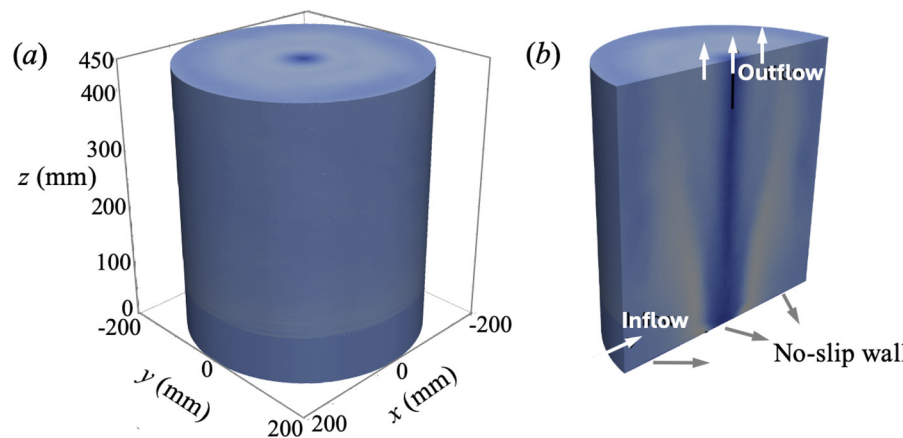


FIG. 2. (a) General illustration of the domain geometry and (b) a schematic of boundary conditions for the numerical setup.

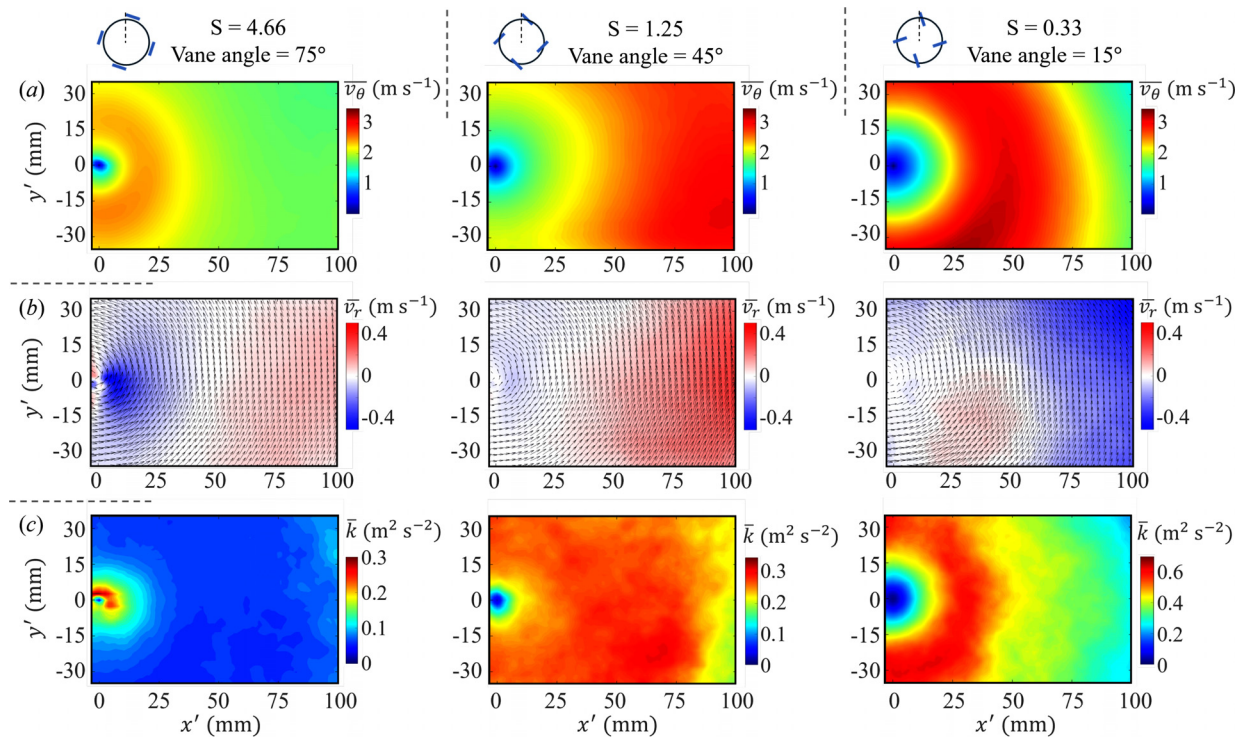


FIG. 3. Time-averaged (a) tangential velocity, v_θ ; (b) radial velocity, v_r , superimposed with in-plane velocity vectors; and (c) turbulent kinetic energy, k , at swirl ratios $S = 4.66$, 1.25 , and 0.33 at $z = 120$ mm, obtained from experiments.

28 May 2025 01:37:14

given moment was determined following Graftieaux *et al.*,⁴² which employs Γ_1 to pinpoint the vortex center. Γ_1 is a dimensionless scalar bound by 1 in absolute value and typically peaks at the vortex center in cases of an axisymmetric, dominant vortex, defined by

$$\begin{aligned} \Gamma_1(\mathbf{P}) &= \frac{1}{\Omega} \int_{M \in \Omega} \frac{(\mathbf{PM} \wedge \mathbf{U}_M) \cdot \hat{\mathbf{k}}}{||\mathbf{PM}|| \cdot ||\mathbf{U}_M||} dS \\ &= \frac{1}{\Omega} \int_{\Omega} \sin(\theta_M) d\Omega, \end{aligned} \quad (1)$$

where Ω represents a region within the measurement plane, \mathbf{P} is the point under interrogation, \mathbf{M} is an arbitrary location within Ω , \mathbf{PM} is the position vector from \mathbf{P} to \mathbf{M} , $\hat{\mathbf{k}}$ is the unit vector normal to the measurement plane, and θ_M is the angle between the position vector \mathbf{PM} and the velocity vector \mathbf{U}_M at M . This configuration yields positive Γ_1 values for counterclockwise flow, as shown in Fig. 3.

The analysis of mean flow statistics demonstrates significant modulations attributable to variations in the swirl ratio. The tangential velocity, denoted as v_θ , tends to increase as the swirl ratio decreases, a relationship clearly depicted in Fig. 3(a). This trend correlates strongly with a more pronounced radial inflow, as shown in Fig. 3(b), where inflow is represented in blue and outflow in red. In-plane turbulent kinetic energy (TKE), given by $\langle u'^2 + v'^2 \rangle / 2$, where u' and v' are the velocity fluctuations in the x and y directions, is illustrated in Fig. 3(c). Regarding turbulent kinetic energy, a lower swirl ratio is linked to increased TKE and a broader spread of significant velocity fluctuations. Conversely, at the highest swirl ratio ($S = 4.66$), TKE is more localized

near the vortex center, with minimal velocity fluctuations observed in the peripheral regions. Regions exhibiting high TKE typically coincide with zones of intense tangential velocity, signaling strong vortical activity.

In the simulations, vortex center wandering was also observed, albeit significantly less, as evidenced by the instantaneous velocity snapshots (omitted here for brevity). This reduced wandering is likely attributable to the idealized slip-wall boundary conditions employed in the simulations, which minimize interactions with lateral flow and the effects of potential air drafts entering through the sides of the chamber. Also, the radial Reynolds number in the simulations is lower, which may further inhibit vortex wandering. Due to the minimal impact of vortex wandering in the simulations, the vortex center position adjustments were deemed unnecessary. Consequently, temporally and azimuthally averaged velocity and turbulent kinetic energy (TKE, including all components, i.e., $\langle u'^2 + v'^2 + w'^2 \rangle / 2$) values are presented in Fig. 4.

The comparison of the tangential velocity fields depicted in Fig. 4(a) with their experimental counterparts in Fig. 3(a) reveals a good alignment in the range of velocities, with peak velocities reaching between 2 and 3 m/s for all cases. This observation confirms that the inlet velocity set at $|v|_{inlet} = 1.4$ m/s in the simulations effectively established a comparable range of velocity values. However, an analysis of peak tangential velocities across the cases illustrates a lack of a consistent trend in peak magnitudes of tangential velocity with decreasing swirl ratio in the simulations; the trend first shows an increase and then a decrease. This pattern can be attributed to the counteracting

effects of the radial Reynolds number, which increases with a decrease in the swirl ratio and tends to elevate tangential velocities²⁴ and a decrease in $v_{\theta,\text{inlet}}$ due to the boundary conditions employed.

Furthermore, the radius of the vortex core, defined here as the radial location where peak tangential velocity occurs, decreases as the swirl ratio diminishes. Previous studies have established a correlation between higher swirl ratios and larger vortex core radii,^{8,26,29} supporting the observations noted in this study.

The radial velocity fields given in Fig. 4(b) generally show low values as one approaches the vortex center. The radial velocity would vanish at the center in an ideal, axisymmetric, radially converging flow. However, centrifugal resistance counteracts this horizontal convergence in the presence of swirling motion, pushing the equilibrium zone—where radial velocities approach zero—outward. Consequently, the larger the swirl, the greater the centrifugal force, which extends the region of near-zero radial velocities further from the center.

Transitioning from the inner to the outer vortex core, the radial velocity begins to increase. The radial velocity can become positive within the outer core, although its magnitude remains low. The radius of the vortex core, identified where the tangential velocity peaks, typically aligns with the position of the peak outward radial velocity, as demonstrated in Fig. 4. This study finds good agreement with experimental observations regarding radial velocities. Consistent with

experimental results, the inflow region (characterized by negative radial velocity) predominates at the outer boundary for a low swirl ratio, whereas an outflow region (positive radial velocity) becomes more dominant for a high swirl ratio at the same boundary.

In numerical simulations, turbulent kinetic energy (TKE) is predominantly concentrated within a ring inside the vortex core for $S = 4.66$ and 1.25 , as shown in Fig. 4(c). For $S = 0.33$, TKE is concentrated at the center, aligning with the observation that the vortex core is narrow and primarily confined to the center for this swirl ratio [Fig. 4(a)]. The localization of TKE peaks within the vortex core can be attributed to high levels of vertical shear induced by radial gradients of vertical velocities.

The pattern of increased TKE levels within the vortex core observed in the simulations generally corresponds with experimental findings, although discrepancies arise from variations in core radii measured in simulations and experiments. Furthermore, consistent with experimental results, lower swirl ratios are associated with higher TKE levels, a phenomenon likely linked to the increased shear resulting from decreased core radii. This effect is potentially amplified in simulations due to an increase in radial Reynolds number with decreasing swirl ratio.

Figure 5 displays the time-averaged vertical and horizontal velocities within the vertical plane that intersects the geometric center of the

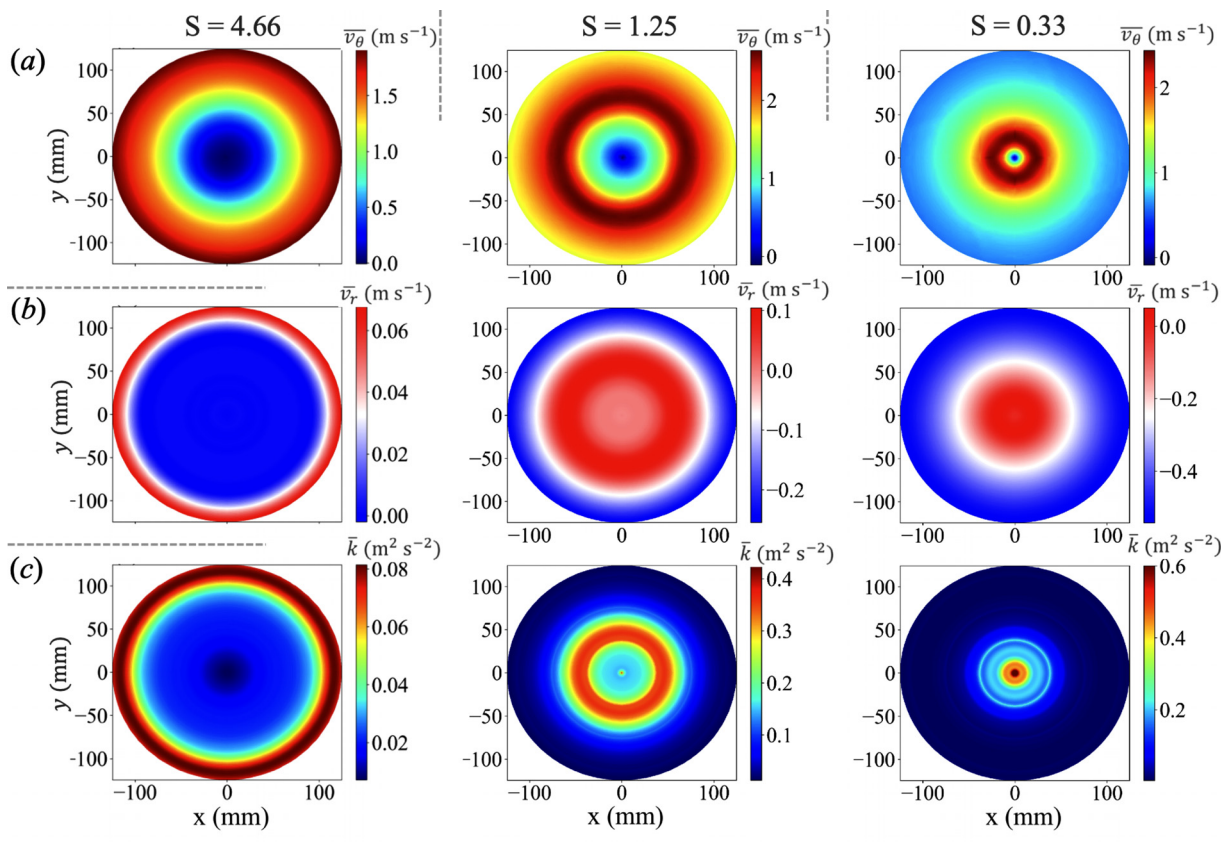


FIG. 4. Time-averaged and azimuthally averaged (a) tangential velocity, v_θ ; (b) radial velocity, v_r ; and (c) turbulent kinetic energy, k , at swirl ratios $S = 4.66$, 1.25 , and 0.33 at $z = 120$ mm from numerical simulations.

system, as obtained in the experiments. It is important to note that the position of the time-averaged vortex center exhibits some low-frequency vortex wandering. However, this should be considered a secondary effect, and the observed patterns are deemed representative. Variations across the cases can be primarily attributed to changes in swirl ratio and, to a lesser extent, to the relative spatial positioning of the vortex center.

For a swirl ratio of $S = 4.66$, the flow pattern is particular, characterized by an extensive region of downward flow forming a localized vortical structure at lower heights, as depicted in Fig. 5(a). As the swirl ratio decreases, these pronounced downward flow patterns diminish, resulting in narrower regions of downward flow at reduced elevations. A comparative analysis of the flow patterns for a swirl ratio of $S = 0.33$ shows a dominance of vertical flow over horizontal flow, highlighting the significant impact of the swirl ratio on flow dynamics.

The averaged vertical and horizontal (radial) velocities from simulations, as depicted in Fig. 6, exhibit consistent patterns, more so than their experimental counterparts. This consistency arises from reduced vortex wandering, previously noted, in conjunction with azimuthal averaging. The flow patterns delineate two distinct regions: the convective zone and the vortex core. Within the convective zone, markedly high positive vertical velocities occur alongside significant radial velocities, which may be positive or negative depending on the elevation. The transition from negative to positive radial velocities with increasing height is attributed to the expansion of the vortex core driven by turbulent entrainment. This expansion propels more fluid outward, culminating in an outward radial flow. Vertical velocities inside the

vortex core are negative, indicating a downdraft. The downdraft regions within the vortex core were also observed in the experiments [Fig. 5(a)], with stronger off-centering due to a vortex wandering but showing similar trends of an increasing width with an increasing swirl ratio.

Time-averaged velocities measured in a horizontal plane, as shown in Fig. 4, were captured at a plane of 120 mm. Here, the radial flow is inward for $S = 0.33$ and 1.25, and outward for $S = 4.66$, corresponding with observations in Fig. 4(b). The core expansion with elevation is more pronounced at lower swirl ratios, characterized by a steeper increase in the core radius due to enhanced turbulence levels at these ratios, promoting more turbulent mixing. In contrast, this effect is diminished in the experimental results shown in Fig. 5, where significant vortex wandering combined with time averaging across the vertical plane tend to moderate this phenomenon.

B. Vortex wandering effects

Vortex wandering, a prominent characteristic of tornado-like vortices, refers to the stochastic movements of the vortex center around its average position. In our experiments, this behavior was analyzed by tracking the instantaneous locations of the vortex center, as illustrated in the scatter distribution shown in Fig. 7(a), derived from FOV1. The position of the vortex center was identified as the location of the maximum of Γ_1 from Eq. (1). In the case of multiple vortices as discussed in Sec. IV D, this would point to the location of the dominant vortex. The magnitude of the wandering was quantified using the

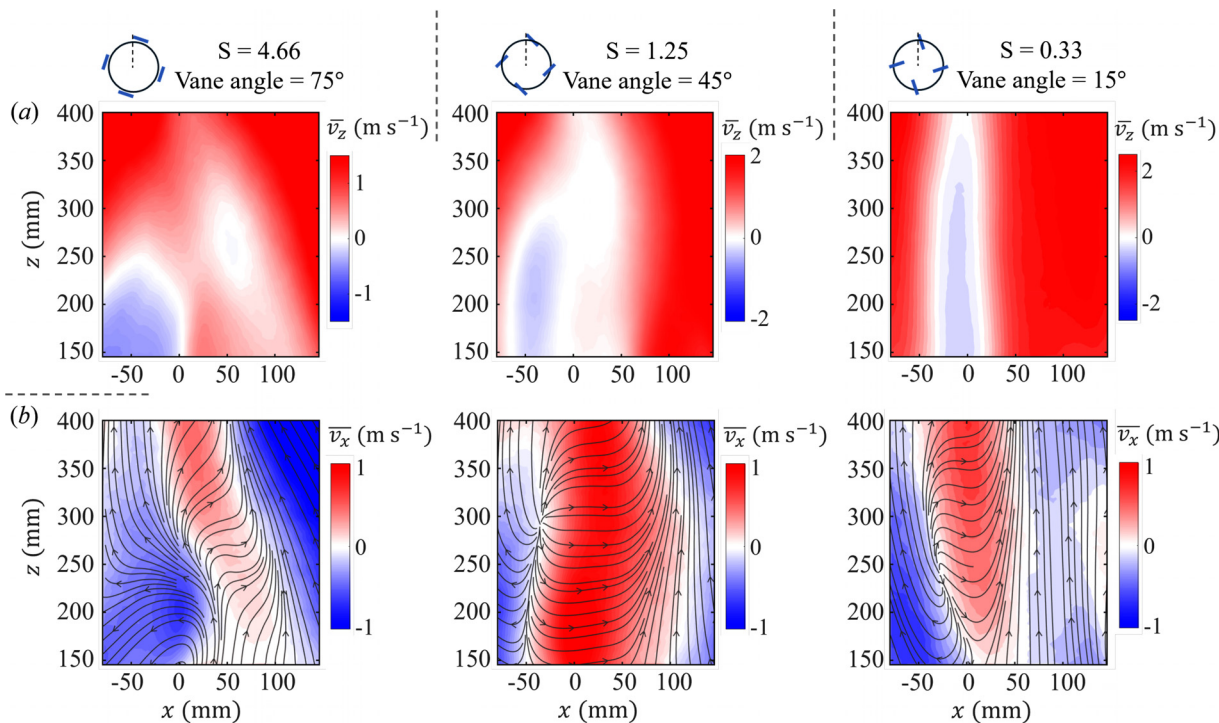


FIG. 5. Time-averaged (a) vertical velocity, v_z and (b) horizontal velocity, v_x , superimposed with streamlines in a vertical plane for swirl ratios of $S = 4.66$, 1.25, and 0.33, obtained from experiments.

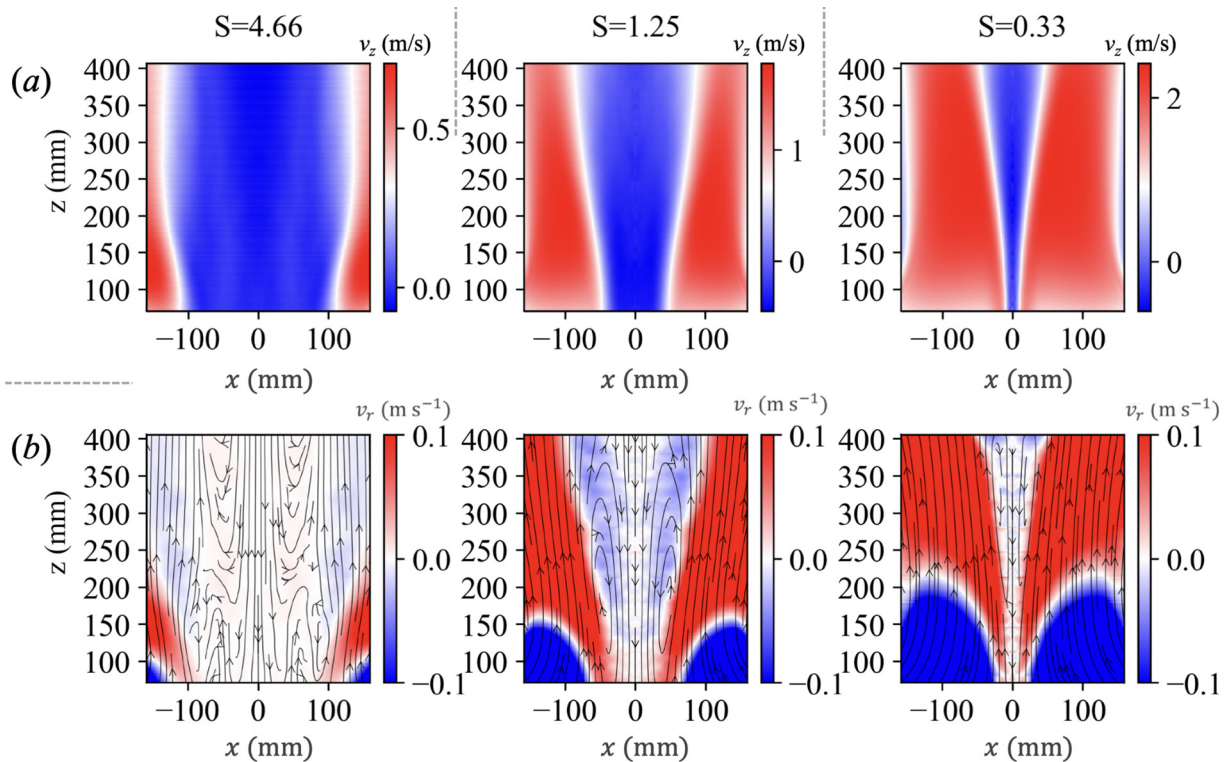


FIG. 6. Time-averaged and azimuthally averaged (a) vertical velocity, v_z and (b) radial velocity, v_r , superimposed with streamlines in a vertical plane at swirl ratios $S = 4.66$, 1.25, and 0.33 from numerical simulations.

28 May 2025 01:37:14

parameter r_w , which represents the distance between the instantaneous and the time-averaged positions of the vortex center. The wandering was most significant at a swirl ratio $S = 1.25$, with a mean value of $\bar{r}_w = 11.9$ mm, compared to $\bar{r}_w = 9.6$ mm and $\bar{r}_w = 9.4$ mm observed at $S = 4.66$ and $S = 0.33$. The probability distributions of r_w , depicted in Fig. 7(b), exhibit a skewed distribution with a longer tail extending toward larger values across the tested cases. The location of the vortex center remained predominantly asymmetric throughout the experiments at the lowest swirl ratio, $S = 0.33$.

As noted, vortex wandering in the simulations was negligible, attributable to the combined effects of a lower radial Reynolds number and idealized boundary conditions that minimize interactions with the surrounding air. Consequently, this phenomenon is not analyzed further in this study.

C. Tangential and radial velocity profiles

Characterization of tornado-like vortices often involves measuring the maximum tangential velocity, denoted as $v_{\theta,\max}$, and its corresponding radius, $r_c = r(v_{\theta,\max})$. Accurately accounting for vortex wandering is essential to avoid underestimating tangential velocity and overestimating vortex size due to smoothing effects.⁴³ Figure 8 presents radial profiles of ensemble-averaged tangential and radial velocities, adjusted relative to the instantaneous vortex center for each frame, as obtained from FOV2 in the experiments (at the $z = 120$ mm horizontal plane). The tangential velocity profile demonstrates a linear pattern near the core, indicative of typical solid-body rotation, followed by a

gradual decline beyond the peak value. Within the inset of Fig. 8(a), the normalized tangential velocity, $v_{\theta}^* = v_{\theta}/v_{\theta,\max}$, in relation to the normalized radial position, $r^* = r/r_c$, is juxtaposed with two analytical models: the Rankine vortex model⁴⁴ and the Burgers–Rott model.^{45,46} The Rankine model, representing the simplest formulation of an ideal vortex, shows a sharp transition from solid-body rotation to a free vortex. Conversely, the Burgers–Rott model, which incorporates radial flow and viscosity considerations, provides a more detailed, smoother transition.⁴⁷ When $r^* < 1$, v_{θ}^* closely aligns with these analytical models, particularly displaying a closer correspondence with the Burgers–Rott model at $S = 0.33$. At higher swirl ratios ($S = 1.25$ and 4.66), v_{θ}^* manifests a marked increase, diverging from both models. For $r^* > 1$, the profiles of v_{θ}^* at $S = 0.33$ and 1.25 align closely with each other and are comparable to the Burgers–Rott model, though v_{θ}^* extends only up to $r^* = 1.5$ at $S = 1.25$ due to the significant value of r_c at this swirl ratio. At $S = 4.66$, v_{θ}^* shows a less pronounced decline, indicating potential deviations from the analytical models, particularly at very high swirl ratios ($S > 2$, a range seldom examined in prior research where $S \leq 1$).

Radial profiles of temporally averaged and azimuthally averaged tangential velocity from numerical simulations are presented in Fig. 9(a) at $z = 120$ mm. As corroborated by Fig. 4, two main observations emerge: (1) the core radius monotonically increases with an increase in the swirl ratio, aligning with previous studies,^{8,26,29} and (2) the maximum tangential velocity remains relatively constant across the three cases, without displaying any consistent monotonic trends.

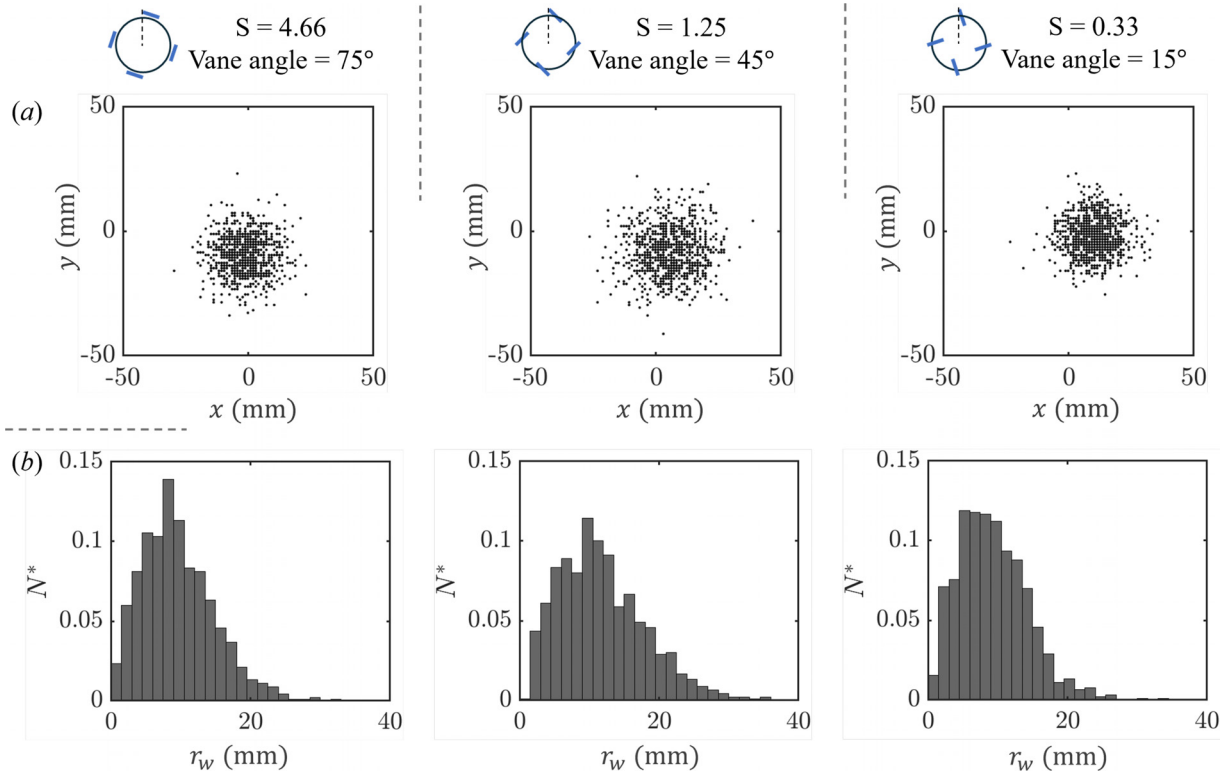


FIG. 7. (a) Instantaneous position of the vortex center and (b) probability distribution of the distance between the time averaged vortex center and the instantaneous vortex center at various swirl ratios $S = 4.66, 1.25$, and 0.33 in experiments from FOV1.

28 May 2025 01:37:14

In Fig. 9(b), the radial profiles of normalized tangential velocity, v_θ^* , demonstrate good agreement with the Burgers–Rott model for both $r^* < 1$ and $r^* > 1$ at $S = 0.33$, similar to experimental observations. Interestingly, the higher two swirl ratios ($S = 1.25$ and 4.66) exhibit a closer fit to the idealized Rankine model, diverging from experimental patterns. The normalized data for $S = 4.66$ are presented only for $r^* < 1.2$ due to the large r_c in simulations for this swirl ratio. The adherence of the $S = 0.33$ profile to the Burgers–Rott model can be attributed to high levels of turbulent mixing, which facilitates radial diffusion of angular momentum effectively captured by this model. This correlates with the high TKE levels and significant vortex core

expansion with height at $S = 0.33$, indicative of substantial turbulent diffusion. For $S = 1.25$ and 4.66 , significantly reduced TKE levels in simulations [Fig. 4(c)] and a less pronounced vortex core spread with height [Fig. 6(a)] diminishes the impact of turbulent viscosity on the v_θ^* profile, resulting in a better fit to the Rankine vortex model. This may also be explained by comparatively lower values of radial Reynolds number for these swirl ratios in the simulations. In contrast, in experiments, the TKE levels and, consequently, the eddy viscosity effects remain substantial at $S = 1.25$ and 4.66 , likely due to a higher Re_r and more pronounced vortex wandering. This results in v_θ^* profiles that deviate from a linear fit; in fact, they are fuller than predicted by

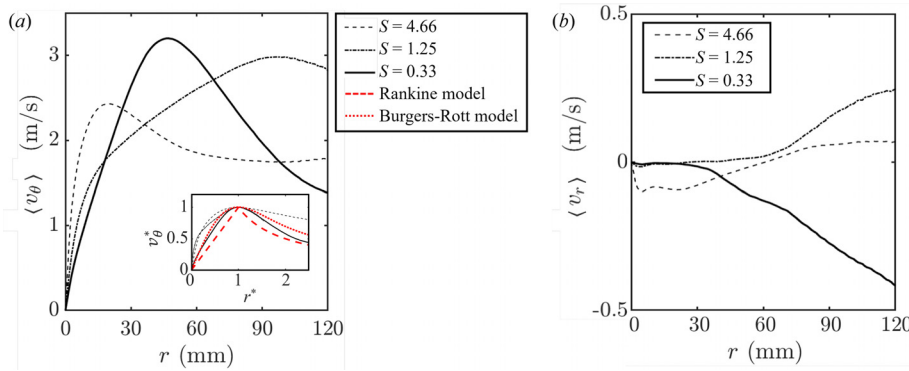


FIG. 8. Radial profiles of ensemble-averaged (a) tangential velocity, v_θ , and (b) radial velocity, v_r , relative to the instantaneous vortex center in each frame, at $z = 120$ mm from experiments. The inset displays normalized tangential velocity, v_θ^* , relative to normalized radial positions at maximum tangential velocity, $r^* = r/r_c$.

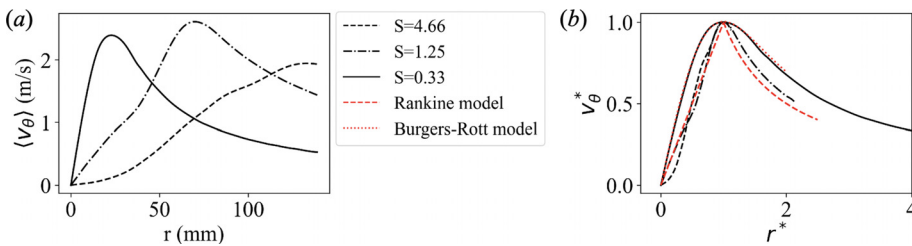


FIG. 9. Radial profiles of time-averaged and azimuthally averaged (a) tangential velocity, v_θ , and (b) normalized tangential velocity, v_θ^* , relative to the normalized radial positions at maximum tangential velocity, $r^* = r/r_c$, at $z = 120$ mm from numerical simulations.

the Burgers-Rott model, potentially because turbulent mixing due to vortex wandering is even more intense than that caused by shear.

Radial velocity profiles, depicted in Fig. 8(b) for experiments measured at $z = 120$ mm, exhibit substantially lower magnitudes compared to their tangential counterparts and show significant variations in magnitude and direction, which are heavily influenced by the swirl ratio. Typically, as the swirl ratio decreases, the magnitude of radial velocity increases, and radial inflow becomes more pronounced relative to outflow at this elevation. This phenomenon is primarily attributed to the reduced vane angle, which facilitates a more favorable pathway for radial inflow. At swirl ratios $S = 0.33$ and $S = 1.25$, a clear transition is observed from minimal radial motion near the vortex core to significant radial inflow or outflow in the outer regions. Although of lower magnitude, at $S = 4.66$, the radial velocity profile shows inflow at the core and outflow at the outer regions with comparable magnitudes. The occurrence of radial inflow at the vortex center at $S = 4.66$, as opposed to the other cases, might be explained by a relatively low tangential velocity in this scenario [as shown in Fig. 8(a)], which does not provide enough centrifugal resistance, as discussed in Sec. IV A, to counterbalance the radial inflow toward the vortex center. It is important to note that quantifying radial velocities, especially close to the vortex center, presents greater challenges than tangential velocities due to their sensitivity to the geometry and scale of the simulator.

Radial profiles in the simulations, as illustrated in Fig. 10(a) for $z = 120$ mm, demonstrate consistent behavior across all three swirl ratios due to mechanisms detailed in Sec. IV A. Specifically, velocities inside the vortex core are determined by a dynamic interplay between radial convergence (radial inflow) and centrifugal resistance (radial outflow), with the latter becoming dominant and accounting for low positive radial velocity bumps at the outer edges of the vortex core. This radial outflow gradually transitions into radial inflow outside the

outer vortex core at this height for the lowest two swirl ratios, $S = 0.33$ and $S = 1.25$. The field of view does not extend far enough to observe such a transition for $S = 4.66$.

A comparison of the radial velocity distributions between the experiments and simulations reveals differences at the swirl ratio $S = 4.66$. These variations may be attributed to the high vane angle of 75° used in the experiments, which, as discussed in Sec. V, could limit the ability to establish the intended boundary conditions. This effect may also contribute to the differences observed in the vortex core radius between the experimental and numerical results, as shown in Figures 3 and 4 for $S = 4.66$. At $S = 1.25$, both approaches exhibit a similar trend, with radial velocity transitioning from minimal values near the center to positive values at larger radial positions. In the simulations, a region of negative radial velocity appears near the outer boundary, which may lie beyond the experimental field of view. For $S = 0.33$, both simulations and experiments indicate the presence of a positive radial velocity near the core, although the magnitude remains low. It is also important to note that the radial velocity is an order of magnitude smaller than the tangential velocity, making it more susceptible to experimental uncertainty and noise. These factors collectively contribute to differences between the measured and simulated radial velocity fields.

To explore whether the radial velocity profiles in the simulations would align if normalized with the maximum radial velocity, $v_{r,\max}$, and the vortex core radius, r_c , Fig. 10(b) presents the normalized radial velocity $v_r^* = v_r/v_{r,\max}$ vs $r^* = r/r_c$. A reasonable collapse is observed, indicating that the vortex core radius, defined by the maximum tangential velocity, essentially coincides with the location of maximum radial velocity for $S = 0.33$ and $S = 1.25$, but not for $S = 4.66$. This discrepancy for $S = 4.66$ may be partially due to a comparatively lower radial Reynolds number, Re_r , just above the critical threshold for

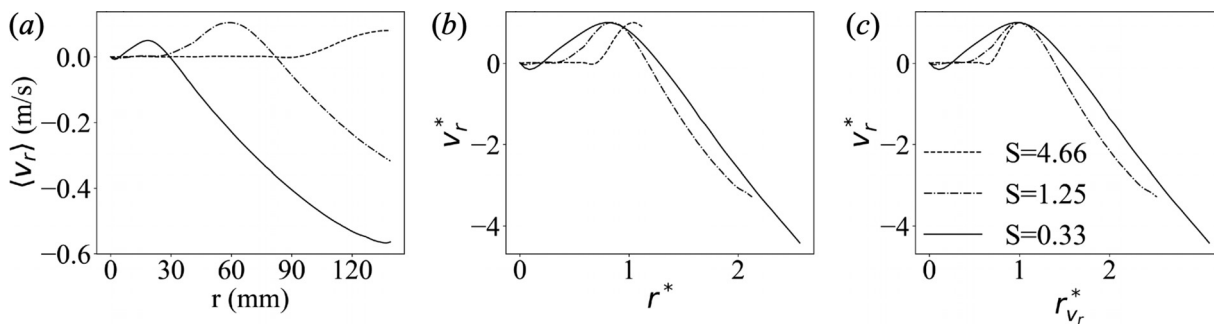


FIG. 10. Radial profiles of time-averaged and azimuthally averaged (a) radial velocity, v_r , (b) normalized radial velocity, v_r^* , relative to the normalized radial positions at maximum tangential velocity, $r^* = r/r_c$; and (c) normalized radial velocity, v_r^* , relative to the normalized radial positions at maximum radial velocity, $r_{v_r}^* = r/r(v_{r,\max})$, at $z = 120$ mm from numerical simulations.

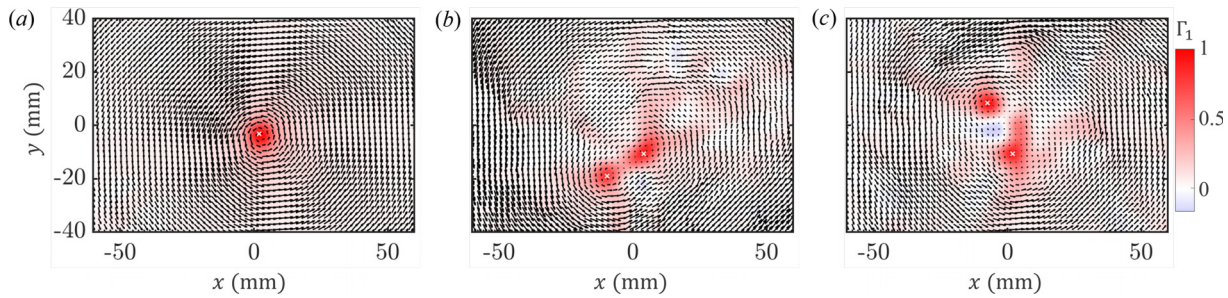


FIG. 11. Instantaneous velocity field superimposed with Γ_1 for $S =$ (a) 4.66, (b) 1.25, and (c) 0.33 from experiments. Cross symbols denote the vortex cores.

turbulent flow, potentially leading to distinct flow patterns within the vortex core from the other two cases.^{28,31}

Further refinement is shown in Fig. 10(c), where the normalized radial velocity $v_r^* = v_r/v_{r,\max}$ is plotted against the radial coordinate normalized by the radial location of the maximum radial velocity, $r_{v_r}^* = r/r(v_{r,\max})$. This adjustment improves the profile collapse, though deviations persist. The good alignment of radial velocity profiles when normalized across all three swirl ratios suggests that it is easier to establish vortex flow regimes, which are close to self-similar, in the simulations, due to an idealized nature of the geometrical setup and boundary conditions. The idealized vortices, realized in numerical simulations, do not account for interactions with the surrounding atmosphere and minimize the effects of vortex wandering and other disturbances common to open-domain experimental setups. This is an essential consideration when comparing experimental results with simulation data.

D. On the coherent vortex structure

The experiments reveal the transient occurrence of double-celled vortical motions within the tornado-like vortex under specific conditions. These flow structures were transient yet influenced by the swirl ratio, S . Figure 11 displays the instantaneous velocity fields overlaid with the Γ_1 function,⁴² calculated from Eq. (1) with Ω defined as a square region of $8 \times 8 \text{ mm}^2$ centered at point P , for three distinct swirl ratios derived from experimental data. In scenarios where $S = 4.66$, a consistent single vortex structure was observed throughout the experimental sessions. In contrast, for $S = 1.25$ and $S = 0.33$, double-celled

vortex structures were detected in approximately 5% and 15% of the observations, respectively.

Additional insights are derived from analyzing the circulation as a function of radial distance, as shown in Fig. 12 for the double-celled vortex observed at a swirl ratio of $S = 0.33$. The instantaneous velocity field captures two co-rotating vortices marked by cross symbols at their centers. Both vortices exhibit comparable circulation magnitudes, with distinct inflection points observed at a curve radius of $r_i = 16 \text{ mm}$, where each curve approaches its counterpart vortex, as illustrated by the circles in Fig. 12(a). Moreover, the circulation calculations were conducted relative to the midpoint of the two vortex centers, as depicted in Fig. 12(c). Circulation remains minimal until reaching a curve radius of $r = 7 \text{ mm}$, beyond which it begins to encompass the influence of the two co-rotating vortices, highlighting the dynamic interaction between them.

The transition between a single vortex and double-celled vortex in experiments was further explored by applying a proper orthogonal decomposition (POD). For a given velocity field $\mathbf{u}(x, y, t)$, POD decomposes it into a series of spatial modes $\phi_n(x, y)$ that represent the coherent structure of the flow field and corresponding temporal coefficients $a_n(t)$, which capture the time-dependent behavior associated with each mode,

$$\mathbf{u}(x, y, t) = \sum_{n=1}^N a_n(t) \phi_n(x, y), \quad (2)$$

where N is the number of snapshots. The spatial modes $\phi_n(x, y)$ are obtained using the method of snapshots, where an eigenvalue

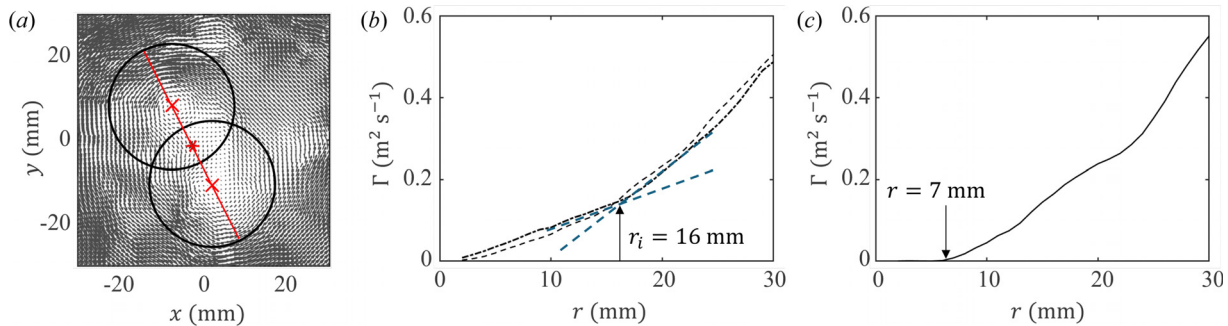


FIG. 12. (a) Instantaneous velocity field displaying a double-celled vortical structure for a swirl ratio of $S = 0.33$ from experiments. Vortex cores are marked with red cross symbols, and the star symbol indicates the midpoint between them. Solid lines represent curves with a radius of $r_i = 16 \text{ mm}$ from each vortex center, highlighting the point where the circulation trend changes. (b) Circulation as a function of radial distance for each vortex. (c) Circulation measured at the midpoint between the two vortex centers.

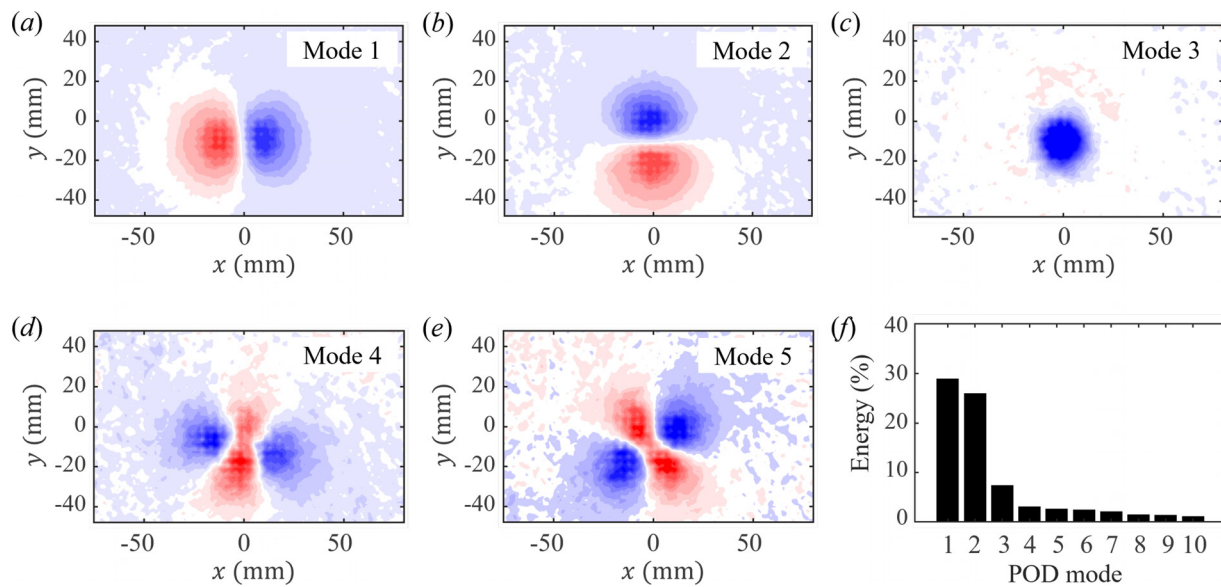


FIG. 13. (a)–(e) First five POD modes of the vorticity field and (f) mode energy distribution for the scenario with swirl ratio of $S = 4.66$ from experiments.

decomposition is applied to the temporal correlation matrix formed from the velocity field snapshots. The resulting eigenvectors are then projected back onto the data to construct the spatial modes, which are orthonormal and ordered by their energy content. The normalized energy content, E_n , is obtained by dividing the eigenvalue of a particular mode by the sum of all N eigenvalues, i.e., $E_n = \lambda_n / \sum_{i=1}^N \lambda_i$, interpreted as the single-mode contribution to the total energy.

Figures 13–15 illustrate the first five POD modes of the vorticity field in FOV1, derived by computing the curl of the POD modes of the velocity components after the mean values have been

subtracted. For the scenario with a swirl ratio of $S = 4.66$ (Fig. 13), the first five POD modes display patterns markedly similar to those of a synthetic single vortex exhibiting Gaussian random wandering, as noted by Karami *et al.*³⁴ The initial two modes are primarily associated with vortex wandering, the third mode distinctly represents the single vortex structure, and the subsequent modes do not contribute significantly to the total energy. This is detailed in the mode energy distribution shown in Fig. 13(f), which points out that vortex wandering dominates the flow's energy, accounting for over 50% of the total energy.

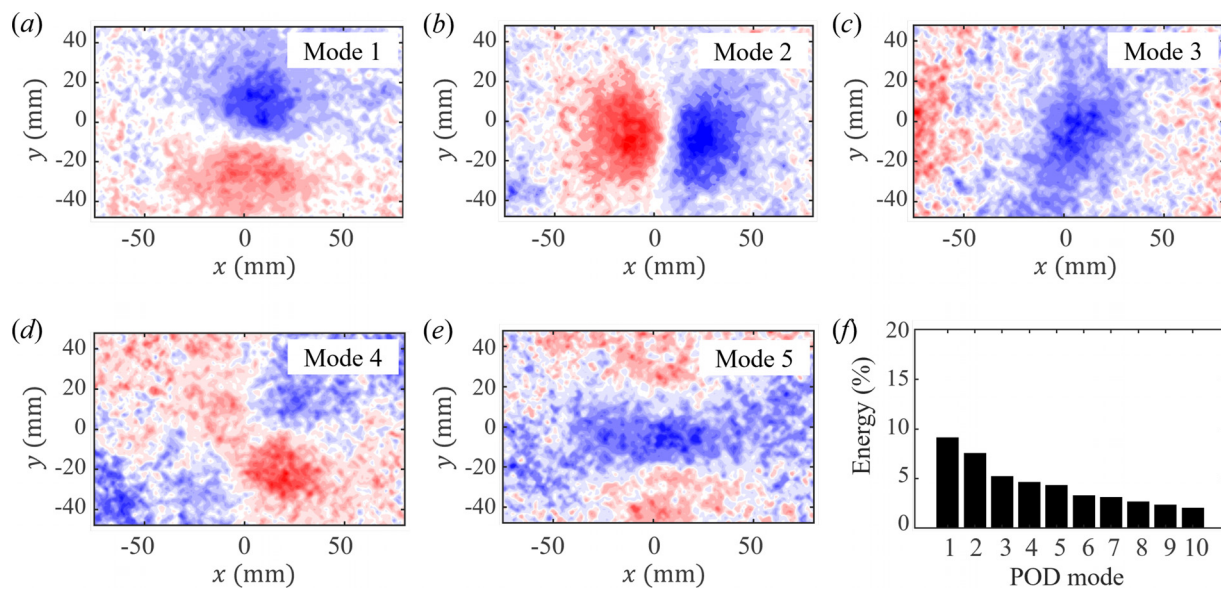


FIG. 14. (a)–(e) First five POD modes of the vorticity field and (f) mode energy distribution for the scenario with swirl ratio of $S = 1.25$ from experiments.

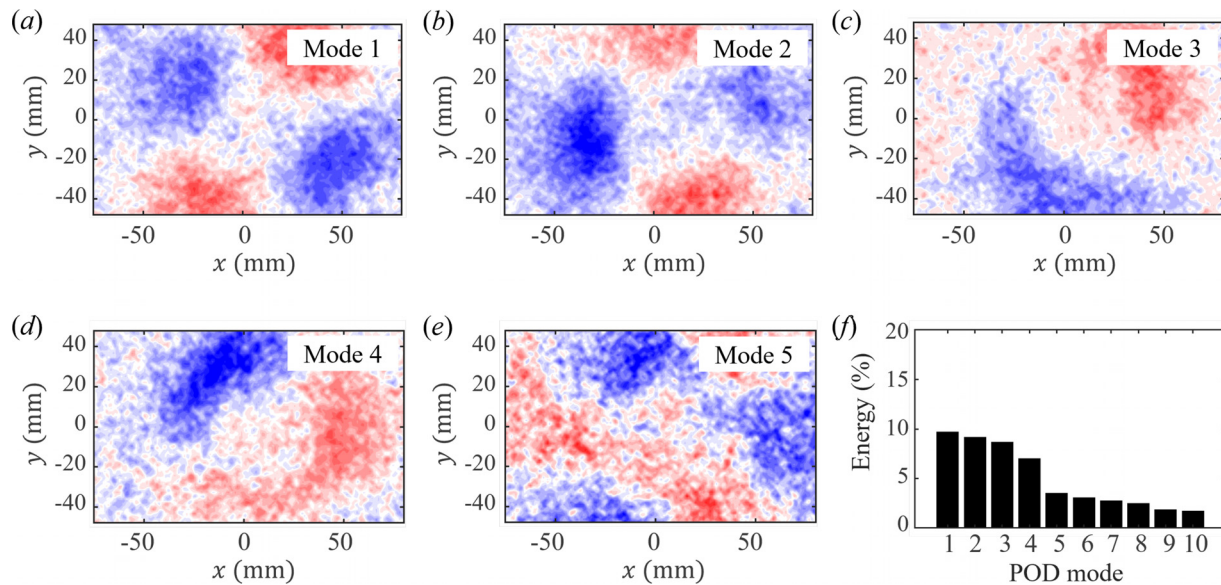


FIG. 15. (a)–(e) First five POD modes of the vorticity field and (f) mode energy distribution for the scenario with swirl ratio of $S = 0.33$ from experiments.

For the swirl ratio of $S = 1.25$ (Fig. 14), the POD modes continue to reflect patterns similar to those observed at $S = 4.66$, though the energy contribution is less. At $S = 0.33$ (Fig. 15), the first two modes mirror the fourth and fifth modes observed in the $S = 4.66$ scenario, with the following two modes indicative of vortex wandering. Interestingly, the fifth mode closely resembles the first mode of a synthetic double spiral vortex as described in Karami *et al.*,³⁴ suggesting the emergence of a double-celled vortex structure contributing significantly to the energy within the flow, although this mode is not dominant at this swirl ratio.

In simulations, coherent vortex structures were identified by analyzing the instantaneous pressure fields, which serve as a reliable indicator of the vortex formation pattern due to a high correlation between low-pressure regions and vortex cores. Figure 16 displays representative snapshots of the instantaneous pressure fields at a horizontal plane near the bottom surface of the domain across three different swirl ratios.

For $S = 0.33$, a single vortex structure is consistently observed at the domain center, which reaffirms the minimal vortex wandering within the simulations. At $S = 1.25$, between two and four vortex structures are typically formed, featuring one primary vortex at the center, surrounded by additional vortices that rotate around it. When the swirl ratio increases to $S = 4.66$, multiple secondary vortices are seen forming around the main vortex core, indicating a complex interaction of rotational flows at higher swirl ratios.

V. DISCUSSION

Both the experimental and simulation phases of this study have clarified distinct flow structures and secondary vortex formations, which are particularly influenced by the swirl ratio. To contextualize these findings within the broader field, Table I compiles a summary of pertinent studies on tornado vortex dynamics, detailing their basic configuration parameters and observations regarding the number of vortices.

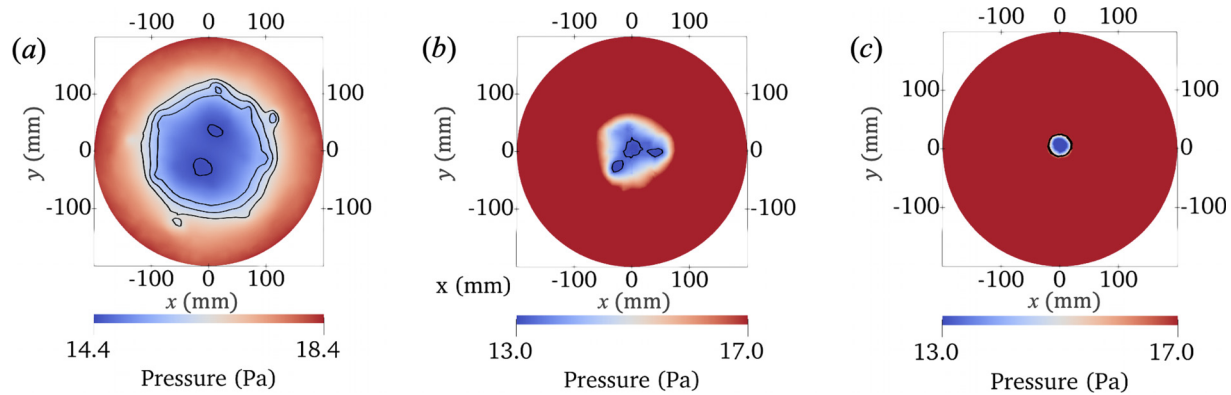


FIG. 16. Instantaneous pressure field snapshots at a horizontal plane for $S =$ (a) 4.66, (b) 1.25, and (c) 0.33 from numerical simulations.

Swirl ratio, a critical parameter in these studies, characterizes the relative amount of tangential momentum to radial momentum within the vortex. This ratio is typically approximated using the inflow angle at the inlet (θ) combined with the aspect ratio (a) of the vortex simulator. It is expressed as $S = (2a)^{-1} \tan(\theta)$, where the aspect ratio $a = h/r_0$ is defined as the ratio of the inflow height (h) to the updraft radius (r_0)—commonly, the radius of the top fan. Here, $\tan(\theta)$ ideally represents the ratio of tangential to radial velocities, $\tan(\theta) = v_\theta/v_r$. This formulation of the swirl ratio is designated as the geometric swirl ratio, S_g , reflecting its reliance solely on geometric parameters.

This geometric interpretation of the swirl ratio originates from Ward-type simulators, which use a rotating wire mesh to induce circulation at the inlet and a direction vane to measure the inflow angle.²⁶ Due to its dependence on geometrically controlled parameters, this definition was adopted in the current study to ensure consistency across experimental and numerical conditions. It has been employed throughout Sec. IV to articulate the dynamics of the vortex formations observed.

Recent advances in tornado chamber designs have led to the elimination of rotating wire meshes and the incorporation of vanes to set the inflow angle, prompting the introduction of alternative swirl ratio definitions based on the ratio of circulation at the inlet to the inflow rate. These definitions are collectively referred to as flow-based swirl ratios, deriving from the reliance on velocity flow data within the vortex to calculate the swirl ratio. For instance, Haan *et al.*⁹ developers of the ISU tornado simulator, introduced a flow-based swirl ratio defined as $S_{f_1} = (\pi r_c^2 v_{\theta,\max})/Q$, where $r_c = r(v_{\theta,\max})$ represents the vortex core radius at the radial location of maximum tangential velocity as defined in Sec. IV C, and Q is the flow rate through the system. This definition was adopted for two primary reasons: (1) the difficulty in defining the updraft radius r_0 in open-type setups such as the ISU simulator and (2) its effectiveness in collapsing results regarding vortex structure across different configurations.

Furthermore, Zhang and Sarkar³² and Liu and Ishihara¹³ utilized this definition in their studies. Another variant, introduced by Refan and Hangan,¹⁷ involves both the updraft radius r_0 and the vortex core radius r_c to define another flow-based swirl ratio as $S_{f_2} = (\pi r_0 r_c v_{\theta,\max})/Q$. The advantage of this definition is that it aligns more closely with the geometric swirl ratio S_g , unlike S_{f_1} , as evidenced in Table I. In their study, Refan and Hangan¹⁷ demonstrated that both S_{f_2} and S_g were comparable up to a vane angle of 40°; beyond this angle, a tornado-like vortex was not achievable, likely due to limitations in the vane setup to deflect flow beyond 40°. The congruence of S_{f_2} and S_g was corroborated in our experiments up to a vane angle of 45° and in simulations across all vane angles.

The data from the current experiments and simulations presented in Table I confirm that the flow-based swirl ratio, S_{f_1} , more effectively collapses data concerning the number of vortices than the geometric swirl ratio, S_g . While S_g suggests a progressive increase in the number of vortices as it rises from 0.33 to 4.66 in simulations, the experimental data exhibit a different trend, reverting to a single-vortex pattern at $S_g = 4.66$. However, this discrepancy is reconciled when considering S_{f_1} ; $S_{f_1} = 0.01$ in experiments at $S_g = 4.66$, which falls within the range indicative of a single-vortex condition, as evidenced by comparisons with other studies in Table I.

The inability of the geometric swirl ratio to reliably differentiate between vortex patterns is further evidenced by the findings of Lv

et al.,³¹ where varying flow patterns were observed for the same S_g , influenced by differences in vane angle and configuration ratio (inverse of the aspect ratio). In terms of the distinctions between S_{f_1} and S_{f_2} , both definitions effectively describe trends in vortex numbers, with lower values of S_{f_2} corresponding to fewer vortices, and higher values indicating more vortices. As suggested by Refan and Hangan,¹⁷ the values of S_{f_2} closely align with S_g under conditions conducive to typical vortex-like flows. When tornado-like vortex flows do not materialize, as in the experiments at a vane angle of 75°, the flow-based swirl ratio S_{f_2} significantly decreases. It can, therefore, be concluded that S_{f_2} serves as an apt indicator of the vortex flow regime, providing values close to S_g under typical vortex conditions while accurately classifying vortex patterns across different regimes.

It is worth discussing the challenges associated with the high vane angle of $\theta = 75^\circ$. This aligns with observations from Refan and Hangan¹⁷ in a comparable experimental setup where top fans provided an updraft and peripheral vanes at the lower chamber controlled the swirl ratio. Refan and Hangan¹⁷ reported that only up to deflection angles of 40° were the vanes effective in directing the flow to produce tornado-like vortex features. Beyond this angle, the pressure distributions and tangential velocity profiles characteristic of vortex flow were absent. This issue may stem from the vanes' inability to adequately deflect the flow at higher angles, potentially causing flow separation from the vanes and failing to maintain the desired flow direction, thereby disrupting the vortex structure.

In contrast, in the simulations, both tangential and radial velocities at the inlet are directly set through boundary conditions without a complication of vane-wall effects, enabling the achievement of the desired inflow angle and the computational formation of vortex-like flows for all investigated inlet angles. It is important to note that the geometric swirl ratio of 4.66 is considerably high and, to the authors' knowledge, has not been previously investigated in experiments, with the highest $S_g = 1.79$ achieved by Leslie²⁷ in the Ward-type apparatus.

VI. CONCLUSIONS

We examined the dynamics of small-scale tornado-like vortices through PIV experiments and numerical simulations across varying swirl ratios, and also inspected the ability of both approaches to generate comparable vortex flow fields under matched conditions, including domain geometry, vane inflow angle, aspect ratio, and geometric swirl ratio. While these parameters were kept consistent, inherent differences between laboratory and numerical models were unavoidable. Simulations employed a slip-wall lateral boundary condition, whereas the experiments allowed for atmospheric interactions. Also, experiments used a hexagonal fan arrangement, while simulations assumed an idealized circular inlet. The radial Reynolds number remained constant in experiments ($Re_r = 3.1 \times 10^4$) but varied in simulations, reaching 4.9×10^3 , 1.3×10^4 , and 1.8×10^4 for swirl ratios of $S = 4.66$, 1.25, and 0.33, respectively. Furthermore, experiments relied on physical guide vanes, while simulations prescribed idealized inlet conditions.

Despite these differences, both approaches successfully established vortex flow fields that aligned well across multiple regimes. Key areas of agreement included tangential and radial velocity magnitudes, normalized tangential velocity profiles, turbulent kinetic energy (TKE) trends, and coherent vortex structures when scaled using the flow-based swirl ratio S_{f_1} . However, discrepancies arose for the highest swirl ratio ($S = 4.66$), where guide vanes in the experiments failed to deflect

TABLE I. Comparative summary of vortex dynamics studies focusing on tornado-like vortices. This table highlights flow parameters and findings from previous research alongside results from the current study. It is important to note that in Ward-type simulators,^{8,27,29} the vane angle θ is not an adjustable parameter but rather a measured quantity.

Configuration ratio, $1/a$	Vane angle, θ	$S_g, \frac{\tan \theta}{2a}$	$S_{f_1}, \frac{\pi r_c^2 v_{\theta,\max}}{Q}$	$S_{f_2}, \frac{\pi r_0 r_c v_{\theta,\max}}{Q}$	Number of vortices	Study
2	$2^\circ - 3^\circ$	0.05	Single vortex	Ward ⁸
2	30°	0.6	Parent vortex + vortex pair	(Experiments)
0.4	75°	0.75	Parent vortex + vortex pair	
1–2	30°	0.3–0.6	Double vortex	Jischke and Parang ²⁹
1–2	40°	0.4–0.8	Double vortex	
1–2	45°	0.5–1	Double vortex	(Experiments)
2	7.5°	0.13	Single vortex	Leslie ²⁷
2	13°	0.23	Transition from single to two vortices	(Experiments)
2	42°	0.90	Transition from 2–3	
2	60°	1.79	Transition to 4	
2	15°	0.26	0.08	...	Single-celled vortices	Haan <i>et al.</i> ⁹
2	55°	1.43	1.14	...	Double-celled vortices	(Experiments)
2	15°	0.26	0.03	...	Single vortex	Zhang and Sarkar ³²
2	45°	1	0.2	...	Multiple vortices	
1.33	46.8°	0.4	0.02	...	Single vortex	(Experiments)
1.33	58°	0.6	0.06	...	Vortex breakdown	Liu and Ishihara ¹³
1.33	69.4°	1.0	0.23	...	Vortex touchdown	(Simulations)
1.33	84.4°	3.8	2.44	...	Multi-vortex	
2.86	5°	0.12	...	0.12	Single vortex	Refan and Hangan ¹⁷
2.86	$15^\circ - 20^\circ$	0.37–0.57	...	0.37–0.57	Vortex breakdown	
2.86	$30^\circ - 40^\circ$	0.96–1.29	...	0.96	Two-celled vortex	(Experiments)
1	20°	0.18	Single vortex	Lv <i>et al.</i> ³¹
2	10°	0.18	Dual-celled vortex	(Experiments)
1	30°	0.29	Single vortex	
2	20°	0.36	Dual-celled vortex	
1	60°	0.87	Single vortex	
2	50°	1.20	Dual-celled vortex	
2	60°	1.73	Dual-celled vortex	
2.3–2.8	32°	0.74–0.88	3 vortices	Zhao <i>et al.</i> ²⁴
3–4	32°	0.95–1.26	4 vortices	(Simulations)
2.5	15°	0.33	0.10	0.40	One or two vortices	Present
2.5	45°	1.25	0.37	0.78	One or two vortices	Experiments
2.5	75°	4.66	0.01	0.13	Single vortex	
2.5	15°	0.33	0.03	0.25	Single vortex	Present
2.5	45°	1.25	0.4	1.13	2–4 vortices	Simulations
2.5	75°	4.66	2.8	4.3	Multiple vortices	

28 May 2025 01:37:14

the flow, preventing tornado-like vortex formation effectively. This aligns with previous studies,¹⁷ which noted the challenge of achieving high swirl ratios experimentally. Conversely, simulations at $S = 4.66$ were influenced by a low radial Reynolds number due to imposed boundary conditions, limiting turbulence development. Alternative

boundary conditions, such as maintaining a constant radial velocity, could mitigate this effect. Nonetheless, the selected LES conditions ensured comparable tangential velocities at the vortex core, facilitating a consistent evaluation of horizontal shear, relevant for sediment entrainment and flux scaling studies.

For $S = 1.25$ and $S = 0.33$, strong agreement between experiments and simulations was achieved. Vortex wandering was significant in experiments, particularly at $S = 1.25$, consistent with prior studies.^{17,31,32} A correction procedure was applied to experimental data, while simulations exhibited minimal wandering, likely due to idealized boundary conditions. The close match between geometrically corrected PIV data and temporally and azimuthally averaged LES results underscores the robustness of the developed PIV/LES comparison framework. Also, proper orthogonal decomposition (POD) identified dominant vortex modes, aiding in the decomposition and refinement of complex vortex structures.

The findings reinforce the suitability of flow-based swirl ratio definitions, particularly S_{f_1} and S_{f_2} , for characterizing vortex structures across experiments and simulations. The collapse of the present results with prior studies (Table I) highlights their utility. Unlike Wang *et al.*,¹⁴ who reported a linear relationship between geometric and flow-based swirl ratios in simulations, this study demonstrates the nonlinear nature of this relationship in physical vortices, emphasizing the need for careful interpretation.

This work provides a foundation for cross-validating PIV and CFD methodologies for unsteady vortex flows and offers insights applicable to large-scale atmospheric vortices. While real tornadoes have a radial Reynolds number on the order of 10^9 to 10^{11} , with a length scale in the kilometer range, multiple studies have shown that once the radial Reynolds number is large enough to ensure turbulent flow, the vortex dynamics become independent of the radial Reynolds number and are primarily a function of the swirl ratio.^{17,28,31} For real tornadoes, the swirl ratio typically ranges from 0.12 to 1.29, which is within the scope of our study. Breakdown of vortices into multi-vortex structures has been documented in real tornadoes.^{48–50} In fact, these subvortices have been associated with a significant damage caused by tornadoes evidenced by narrow streaks of extreme destruction within the broader tornado path. Characterization of the mechanisms that influence subvortices' formation and evolution in laboratory experiments will help understand and mitigate the vortex breakdown effects in real large-scale tornadoes. Another important mechanism that affects the vortex formation and breakdown in real tornadoes is a baroclinic production of vorticity due to temperature gradients that is not considered in the current study. Baroclinically produced vorticity contributes to the vortex circulation and can raise the effective swirl ratio. This can intensify the vortex breakdown and formation of subvortices.^{51–53} Baroclinic effects on the vortex dynamics will be studied in our future work. Future research will also integrate suspended particulate matter into experimental and computational frameworks to explore dust devils and debris-laden tornadoes. PIV combined with particle tracking velocimetry (PTV) and LES may allow for the investigation of unique particle transport mechanisms within vortex flows, contributing to a broader understanding of sediment transport dynamics, air quality implications, and the environmental impact of natural vortical phenomena.

ACKNOWLEDGMENTS

The support for this work has been provided by the National Science Foundation under the Grant Nos. NSF AGS-2207115 and NSF AGS-2207026.

AUTHOR DECLARATIONS

Conflict of Interest

The authors have no conflicts to disclose.

Author Contributions

Soohyeon Kang: Data curation (equal); Formal analysis (equal); Investigation (equal); Methodology (equal); Validation (equal); Visualization (equal); Writing – original draft (equal). **Rajesh Ramesh:** Data curation (equal); Formal analysis (equal); Investigation (equal); Methodology (equal); Validation (equal); Visualization (equal); Writing – original draft (equal). **Yulia Peet:** Conceptualization (equal); Funding acquisition (equal); Investigation (equal); Methodology (equal); Project administration (equal); Supervision (equal); Writing – original draft (equal); Writing – review & editing (equal). **Leonardo P. Chamorro:** Conceptualization (equal); Funding acquisition (equal); Investigation (equal); Methodology (equal); Project administration (equal); Supervision (equal); Writing – original draft (equal); Writing – review & editing (equal).

DATA AVAILABILITY

The data that support the findings of this study are available from the corresponding author upon reasonable request.

REFERENCES

- ¹NOAA, see www.noaa.gov/photo-story-americas-deadliest-year-for-tornadoes-2011 for “America’s deadliest year for tornadoes” (2016) (accessed May 16, 2024).
- ²L. Dong, *Analysis of Spatiotemporal Patterns of Significant Tornado Damages in the United States* (Digital Repository of Nanyang Technological University, 2024).
- ³H. B. Bluestein and J. H. Golden, “A review of tornado observations,” *Geophys. Monogr. Ser.* **79**, 319–352 (1993).
- ⁴P. M. Markowski, J. M. Straka, and E. N. Rasmussen, “Direct surface thermodynamic observations within the rear-flank downdrafts of nontornadic and tornadic supercells,” *Mon. Weather Rev.* **130**, 1692–1721 (2002).
- ⁵C. R. Alexander and J. Wurman, “The 30 May 1998 Spencer, South Dakota, storm. Part I: The structural evolution and environment of the tornadoes,” *Mon. Weather Rev.* **133**, 72–97 (2005).
- ⁶J. Wurman and C. R. Alexander, “The 30 May 1998 Spencer, South Dakota, storm. Part II: Comparison of observed damage and radar-derived winds in the tornadoes,” *Mon. Weather Rev.* **133**, 97–119 (2005).
- ⁷C. A. Wan and C. C. Chang, “Measurement of the velocity field in a simulated tornado-like vortex using a three-dimensional velocity probe,” *J. Atmos. Sci.* **29**, 116–127 (1972).
- ⁸N. B. Ward, “The exploration of certain features of tornado dynamics using a laboratory model,” *J. Atmos. Sci.* **29**, 1194–1204 (1972).
- ⁹F. L. Haan, Jr., P. P. Sarkar, and W. A. Gallus, “Design, construction and performance of a large tornado simulator for wind engineering applications,” *Eng. Struct.* **30**, 1146–1159 (2008).
- ¹⁰M. Refan, H. Hangan, and J. Wurman, “Reproducing tornadoes in laboratory using proper scaling,” *J. Wind Eng. Ind. Aerodyn.* **135**, 136–148 (2014).
- ¹¹D. S. Nolan and B. F. Farrell, “The structure and dynamics of tornado-like vortices,” *J. Atmos. Sci.* **56**, 2908–2936 (1999).
- ¹²L. Kuai, F. L. Haan, Jr., W. A. Gallus, Jr., and P. P. Sarkar, “CFD simulations of the flow field of a laboratory-simulated tornado for parameter sensitivity studies and comparison with field measurements,” *Wind Struct.* **11**, 75–96 (2008).
- ¹³Z. Liu and T. Ishihara, “Numerical study of turbulent flow fields and the similarity of tornado vortices using large-eddy simulations,” *J. Wind Eng. Ind. Aerodyn.* **145**, 42–60 (2015).
- ¹⁴M. Wang, S. Cao, and J. Cao, “Numerical study on applicability of various swirl ratio definitions to characterization of tornado-like vortex flow field,” *J. Wind Eng. Ind. Aerodyn.* **220**, 104841 (2022).

- ¹⁵J. Wurman, J. Straka, E. Rasmussen, M. Randall, and A. Zahrai, "Design and deployment of a portable, pencil-beam, pulsed, 3-cm Doppler radar," *J. Atmos. Oceanic Technol.* **14**, 1502–1512 (1997).
- ¹⁶S. J. Ying and C. Chang, "Exploratory model study of tornado-like vortex dynamics," *J. Atmos. Sci.* **27**, 3–14 (1970).
- ¹⁷M. Refan and H. Hangan, "Characterization of tornado-like flow fields in a new model scale wind testing chamber," *J. Wind Eng. Ind. Aerodyn.* **151**, 107–121 (2016).
- ¹⁸M. Refan and H. Hangan, "Near surface experimental exploration of tornado vortices," *J. Wind Eng. Ind. Aerodyn.* **175**, 120–135 (2018).
- ¹⁹R. Rotunno, "Numerical simulation of a laboratory vortex," *J. Atmos. Sci.* **34**, 1942–1956 (1977).
- ²⁰B. H. Fiedler, "Numerical simulation of axisymmetric tornadogenesis in forced convection," in *The Tornado: Its Structure, Dynamics, Prediction, and Hazards*, edited by C. Church, D. Burgess, C. Doswell, and R. Davies-Jones (American Geophysical Union, 1993), Vol. 79, pp. 41–48.
- ²¹W. S. Lewellen, D. C. Lewellen, and R. I. Sykes, "Large-eddy simulation of a tornado's interaction with the surface," *J. Atmos. Sci.* **54**, 581–605 (1997).
- ²²D. Natarajan and H. Hangan, "Large eddy simulations of translation and surface roughness effects on tornado-like vortices," *J. Wind Eng. Ind. Aerodyn.* **104–106**, 577–584 (2012).
- ²³H. Zhang, Z. Tang, D. Zuo, and D. James, "Numerical simulation of tornado-like vortices generated in a tornado simulator using large eddy simulation," in 14th Americas Conference on Wind Engineering, 2022.
- ²⁴Y. Zhao, G. Yan, R. Feng, H. Kang, and Z. Duan, "Influence of swirl ratio and radial Reynolds number on wind characteristics of multi-vortex tornadoes," *Adv. Struct. Eng.* **26**, 89–107 (2023).
- ²⁵A. Gairola and G. Bitsuamlak, "Numerical tornado modeling for common interpretation of experimental simulators," *J. Wind Eng. Ind. Aerodyn.* **186**, 32–48 (2019).
- ²⁶R. P. Davies-Jones, "The dependence of core radius on swirl ratio in a tornado simulator," *J. Atmos. Sci.* **30**, 1427–1430 (1973).
- ²⁷F. W. Leslie, "Surface roughness effects on suction vortex formation: A laboratory simulation," *J. Atmos. Sci.* **34**, 1022–1027 (1977).
- ²⁸C. R. Church, J. T. Snow, G. L. Baker, and E. M. Agee, "Characteristics of tornado-like vortices as a function of swirl ratio: A laboratory investigation," *J. Atmos. Sci.* **36**, 1755–1776 (1979).
- ²⁹M. C. Jischke and M. Parang, "Properties of simulated tornado-like vortices," *J. Atmos. Sci.* **31**, 506–519 (1974).
- ³⁰Z. Tang, C. Feng, L. Wu, D. Zuo, and D. L. James, "Characteristics of tornado-like vortices simulated in a large-scale Ward-type simulator," *Boundary-Layer Meteorol.* **166**, 327–350 (2018).
- ³¹P. Lv, Y. Zhang, Y. Wang, and B. Wang, "Experimental investigation on the influence of swirl ratio on tornado-like flow fields by varying updraft radius and inflow angle," *Atmosphere* **14**, 1425 (2023).
- ³²W. Zhang and P. P. Sarkar, "Near-ground tornado-like vortex structure resolved by particle image velocimetry (PIV)," *Exp. Fluids* **52**, 479–493 (2012).
- ³³C. R. Church, J. T. Snow, and E. M. Agee, "Tornado vortex simulation at Purdue University," *Bull. Am. Meteorol. Soc.* **58**, 900–909 (1977).
- ³⁴M. Karami, H. Hangan, L. Carassale, and H. Peerhossaini, "Coherent structures in tornado-like vortices," *Phys. Fluids* **31**, 085118 (2019).
- ³⁵D. S. Nolan, "A new scaling for tornado-like vortices," *J. Atmos. Sci.* **62**, 2639–2645 (2005).
- ³⁶D. C. Lewellen, W. S. Lewellen, and J. Xia, "The influence of a local swirl ratio on tornado intensification near the surface," *J. Atmos. Sci.* **57**, 527–544 (2000).
- ³⁷S. Gillmeier, M. Sterling, and H. Hemida, "Simulating tornado-like flows: The effect of the simulator's geometry," *Meccanica* **54**, 2385–2398 (2019).
- ³⁸P. Fischer, J. Lottes, S. Kerkemeier, O. Marin, K. Heisey, A. Obabko, E. Merzari, and Y. Peet, "Nek5000: User's manual," Technical Report No. ANL/MCS-TM-351 (Argonne National Laboratory, 2015).
- ³⁹A. T. Patera, "A spectral element method for fluid dynamics: Laminar flow in a channel expansion," *J. Comput. Phys.* **54**, 468–488 (1984).
- ⁴⁰P. Fischer and J. Mullen, "Filter-based stabilization of spectral element methods," *C. R. Acad. Sci., Ser. I* **332**, 265–270 (2001).
- ⁴¹T. Chatterjee and Y. T. Peet, "Regularization modelling for large-eddy simulation in wall-bounded turbulence: An explicit filtering-based approach," *Int. J. Numer. Methods Fluids* **88**, 1–17 (2018).
- ⁴²L. Graffteaux, M. Michard, and N. Grosjean, "Combining PIV, POD and vortex identification algorithms for the study of unsteady turbulent swirling flows," *Meas. Sci. Technol.* **12**, 1422 (2001).
- ⁴³R. Ashton, M. Refan, G. V. Iungo, and H. Hangan, "Wandering corrections from PIV measurements of tornado-like vortices," *J. Wind Eng. Ind. Aerodyn.* **189**, 163–172 (2019).
- ⁴⁴W. J. M. Rankine, *A Manual of Applied Mechanics* (Charles Griffin and Company, 1872).
- ⁴⁵J. M. Burgers, "A mathematical model illustrating the theory of turbulence," *Adv. Appl. Mech.* **1**, 171–199 (1948).
- ⁴⁶N. Rott, "On the viscous core of a line vortex," *J. Appl. Math. Phys.* **9**, 543–553 (1958).
- ⁴⁷V. T. Wood and L. W. White, "A new parametric model of vortex tangential-wind profiles: Development, testing, and verification," *J. Atmos. Sci.* **68**, 990–1006 (2011).
- ⁴⁸T. T. Fujita, "The Lubbock tornadoes: A study of suction spots," *Weatherwise* **23**, 161–173 (1970).
- ⁴⁹J. Wurman, "The multiple-vortex structure of a tornado," *Weather Forecast.* **17**, 473–505 (2002).
- ⁵⁰H. B. Bluestein, K. J. Thiem, J. C. Snyder, and J. B. Houser, "The multiple-vortex structure of the El Reno, Oklahoma, tornado on 31 May 2013," *Mon. Weather Rev.* **146**, 2483–2502 (2018).
- ⁵¹D. Staley and R. Gall, "Barotropic instability in a tornado vortex," *J. Atmos. Sci.* **36**, 973–981 (1979).
- ⁵²R. J. Trapp, "A clarification of vortex breakdown and tornadogenesis," *Mon. Weather Rev.* **128**, 888–895 (2000).
- ⁵³E. N. Rasmussen, S. Richardson, J. M. Straka, P. M. Markowski, and D. O. Blanchard, "The association of significant tornadoes with a baroclinic boundary on 2 June 1995," *Mon. Weather Rev.* **128**, 174–191 (2000).